Functionality-Based Formation of Secondary Organic Aerosol from *m*-Xylene

Photooxidation

Yixin Li[1,2], Jiayun Zhao[1], Mario Gomez-Hernandez[1], Michael Lavallee[3], Natalie M. Johnson[4],

and Renyi Zhang[1,3*]

[1]Department of Chemistry, Texas A&M University, College Station, TX 77843, USA

[2]Department of Chemistry, University of California Irvine, Irvine, CA 92697, USA

[3]Department of Atmospheric Sciences, Texas A&M University, College Station, TX 77843,

USA

[4]Department of Environmental & Occupational Health, School of Public Health, Texas A&M

University, College Station, TX 77843, USA

ABSTRACT. Photooxidation of volatile organic compounds (VOCs) produces condensable oxidized organics (COOs) to yield secondary organic aerosol (SOA), but the fundamental chemical mechanism for gas-to-particle conversion remains uncertain. Here we elucidate the production of COOs and their roles in SOA and brown carbon (BrC) formation from *m*-xylene oxidation by simultaneous monitoring the evolutions of gas-phase products and aerosol properties in an environmental chamber. Four COO types with the distinct functionalities of dicarbonyls, carboxylic acids, polyhydroxy aromatics/quinones, and nitrophenols are identified from early-generation oxidation, with the yields of 25%, 37%, 5%, and 3%, respectively. SOA formation occurs via several heterogeneous processes, including interfacial interaction, ionic dissociation/acid-base reaction, and oligomerization, with the yields of $(20 \pm 4)\%$ and $(32 \pm 7)\%$ at 10% and 70% relative humidity (RH), respectively. Chemical speciation shows the dominant presence of oligomers, nitrogen-containing organics, and carboxylates at high RH and carboxylates at low RH. The identified BrC includes N-heterocycles/N-heterochains and

24 nitrophenols, as evident from reduced single scattering albedo. The measured uptake coefficient

25 (γ) for COOs is dependent on the functionality, ranging from 3.7×10^{-4} to 1.3×10^{-2}. A

26 functionality-based kinetic framework is developed to predict SOA production from the

27 measurements of the concentrations and uptake coefficients for COOs, which well reproduces

28 SOA formation from *m*-xylene oxidation. Our results reveal that photochemical oxidation of *m*-

29 xylene represents a major source for SOA and BrC formation under urban environments, because

30 of its large abundance, high reactivity with OH, and high yields for COOs.

31 **Corresponding to:** Email: renyi-zhang@tamu.edu

32

33 **1.   Introduction**

34   Photooxidation of anthropogenic and biogenic volatile organic compounds (VOCs)

35 produces tropospheric ozone, secondary organic aerosol (SOA), and brown carbon (BrC), with

36 profound implications for air quality, human health, and climate (Pope et al., 2002; Li et al., 2007;

37 IPCC, 2013; NASEM, 2016; Molina, 2021; Zhang et al., 2021). For example, SOA contributes to

38 the Earth energy budget, directly by scattering solar radiation and indirectly by serving as cloud

39 condensation nuclei to influence cloud formation and precipitation (IPCC, 2013; Wang et al., 2014;

40 Zhu et al., 2017). Also, light absorbing BrC interferes with solar radiation transfer, contributing to

41 positive radiative forcing (Wang et al. 2013; NASEM, 2016). VOC oxidation is initiated by various

42 oxidants (e.g., OH, O_3, NO_3, etc.) and proceeds via multiple pathways and stages (Atkinson, 2000;

43 Suh et al., 2001; Zhang et al., 2002; Zhao et al., 2004; Wennberg et al., 2018), yielding condensable

44 oxidized organics (COOs) to form SOA and BrC via gas-to-particle conversion (Finlayson-Pitts

45 and Pitts, 2000; Moise et al., 2015; Seinfeld and Pandis, 2016). Currently, the enormous chemical

46 complexity for VOC oxidation and gas-to-particle conversion represents one of the greatest

47 challenges in atmospheric chemistry research (Ravishankara, 1997; Zhang et al., 2015; NASEM,

48   2016). Aromatic hydrocarbons (e.g., benzene, toluene, xylenes, and trimethylbenzene) account for

49   20-30% of the total VOCs and are the major anthropogenic SOA precursors in the urban

50   atmosphere (Calvert et al., 2002; Ng et al., 2007; Song et al., 2007; Guo et al., 2014; Seinfeld and

51   Pandis, 2016). For example, m-xylene or $C_6H_4(CH_3)_2$ represents an important type of aromatic

52   hydrocarbons, which is emitted primarily from industrial and traffic sources. The concentration of

53   m-xylene ranges in a level from sub part per billion (ppb) up to several tens of ppb under urban

54   environments (Calvert et al., 2002; Fortner et al., 2009). Photooxidation of m-xylene is primarily

55   initiated by OH with a rate constant of 2.4×10^{-11} cm^3 molecule^{-1} s^{-1}, which is nearly four times

56   higher than that of toluene (Fan and Zhang, 2008; Ji et al., 2017). A laboratory study identified m-

57   tolualdehyde, m-dimethylphenols, and dicarbonyls (i.e., glyoxal, methylglyoxal, unsaturated

58   dicarbonyls, and epoxy carbonyls) as the main gas-phase products from OH-initiated oxidation of

59   m-xylene (Zhao et al., 2005).

60   Several types of COOs with distinct functionality and volatility are produced form m-

61   xylene photooxidation, contributing to aerosol nucleation and grow (Zhang et al., 2004; Zhang et

62   al., 2015; Guo et al., 2020). SOA formation is conventionally considered to be mainly resulted

63   from equilibrium gas-particle partitioning of semi-, intermediate-, or low-volatile products

64   (Shrivastava et al., 2017). Aromatic oxidation by OH yields low-volatile polyhydroxy

65   aromatics/quinones (denoted as PAQ hereafter), which condense to the aerosol-phase (Schwantes

66   et al., 2017). Also, chain autoxidation reactions of RO_2 from aromatics photooxidation likely yield

67   highly oxygenated molecules (HOMs) with low volatility (Molteni et al., 2018; Garmash et al.,

68   2020; Wang et al., 2020), although the reported yield of HOMs from m-xylene oxidation is small

69   (1.0-1.7%) (Molteni et al., 2018). Several key oxidation products of aromatic oxidation have been

70   shown to readily engage in multiphase reactions and contribute to SOA formation (Ji et al., 2020,

71 Li et al., 2021a). A recent experimental study demonstrated that SOA formation from toluene

72 photooxidation is mainly contributed by volatile dicarbonyls and organic acids (Li et al., 2021b).

73 Moreover, the aqueous reactions between small α-dicarbonyls and base species (e.g., ammonia

74 and amines) produce light-absorbing brown carbon (BrC) (De Haan et al., 2011, 2017; Marrero-

75 Ortiz et al., 2019; Li et al., 2021a,b). Previous experimental studies identified the presence of

76 hydroxy (C-OH), carbonyl (C=O), and acetal (C-O-C) functional groups in aromatic-derived SOA

77 formed via aqueous reactions, implicating a role of oxygenated organics in SOA formation (Jia

78 and Xu, 2014; Jia and Xu, 2018; Zhang et al., 2019). Also, laboratory experiments showed that

79 coating of *m*-xylene SOA on black carbon particles significantly enhances scattering, absorption,

80 and single scattering albedo (SSA) (Guo et al., 2016).

81   Current atmospheric models mainly parameterize SOA formation based on equilibrium

82 partitioning for semi- to low-volatile COOs (Shrivastava et al., 2017). However, gas-to-particle

83 conversion corresponds to decreasing entropy (i.e., $\Delta S \ll 0$), representing non-equilibrium

84 chemical processes (Peng et al., 2021). Moreover, the occurrence of particle-phase reactions

85 significantly alters the physiochemical properties (including volatility, hygroscopicity, and optical

86 properties) for COOs (Tan et al., 2012; Faust et al., 2017; Ji et al., 2020; Li et al., 2021a,b; Liu et

87 al., 2021). Notably, the volatility-based approach consistently under-predicts SOA formation

88 (Heald et al., 2005; Zhang et al., 2015; Hodzic et al., 2016), particularly during haze formation

89 under polluted conditions (Guo et al., 2014; Peng et al., 2021). Here we investigate the production

90 of COOs with different functionalities and assess their roles in SOA formation from *m*-xylene

91 oxidation. A primary objective of this work is to establish a functionality-based framework to

92 predict SOA formation from VOC photooxidation.

93 **2.   Experimental Methodology**

2.1 Chamber experiments

The production of COOs and their roles in SOA formation from *m*-xylene oxidation were investigated using a 1 m^3 chamber (Teflon® PFA, Fig. S1 in the Supplementary Information or SI), similar to our previous studies (Li et al., 2021a,b). The environmental chamber was equipped with eighteen black light lamps (18 × 30W, F30T8/350BL, Sylvania). A water bubbler at a temperature of 30°C was used to humidify the chamber to 10%, 30%, 50%, or 70% relative humidity (RH), and all experiments were performed at 298 K. Three types of seed particles were produced using a constant output atomizer (Model 3076, TSI) to represent various chemical compositions, i.e., NH_4HSO_4 - ammonium bisulfate (ABS), $(NH_4)_2SO_4$ - ammonium sulfate (AS) in the presence and absence of NH_3, and NaCl - sodium chloride. Seed particles were dried to RH of ∼2% by a Nafion drier (PD-070−18T-12SS, Perma Pure) and size-selected for an initial size of 100 nm by a differential mobility analyzer (DMA, Model 3081, TSI). Size-selected particles were injected into the chamber with an initial particle concentration of $1.5 × 10^4$ cm^{-3} measured by a condensation particle counter (CPC, Model 3760A, TSI). The acidity of seed particles was estimated using a thermodynamic model (Fountoukis and Nenes, 2007; Wang et al., 2018), with the pH value of 3∼5 in the presence of gaseous NH_3 and 0∼1 in the absence of gaseous NH_3 for $(NH_4)_2SO_4$, -0.5 for NH_4HSO_4, and 7 for NaCl. To investigate the effects of NH_3 and NO_x, commercially available gaseous NH_3 (2000 ppm NH_3 in N_2) and NO_2 (500 ppm NO_2 in air) was injected into the chamber with a flow of 100 sccm. 600 μL H_2O_2 (35 wt%, Sigma-Aldrich) and 10 μL *m*-xylene (99.5%, Sigma-Aldrich) were injected into a glass reservoir, which was then flushed into the chamber by a 10 slpm flow from a pure air generator (Aadco 737-11, Aadco Inc.) for 10 min. The gases were then mixed by a fan inside the chamber. Once desired concentrations were established, the black light lamps were turned on to initiate H_2O_2 photolysis to generate OH

117 radicals. The initial concentration for *m*-xylene and the steady-state concentration for OH were

118 estimated to be 1.9 ppm and 2.1×10^6 molecules cm^{-3}, respectively (Fig. 1a). The experimental

119 conditions are summarized in Table 1.

120 **2.2 Analytical instruments**

121 The particle size growth, density, light scattering/absorption were simultaneously and

122 continuously monitored, after monodispersed seed particles were exposed to the products of *m*-

123 xylene-OH oxidation in the reaction chamber. A scanning mobility particle sizer (SMPS)

124 consisting of a DMA and a CPC was used to continuously measure the particle size growth factor,

125 GF = D_p/D_0, where D_p is the diameter after exposure and D_o = 100 nm is the initial diameter. Note

126 both D_p and D_0 correspond to the dry particle diameter measured after passing through a Nafion

127 dryer (~2% RH). An aerosol particle mass analyzer (APM, Model 3600, Kanomax) was used to

128 derive the particle density throughout the experiments (Li et al., 2021b). The density for the SOA

129 materials (ρ_{SOA}) is calculated by,

$$\rho_{SOA} = \frac{\rho \times GF^3 - \rho_0}{GF^3 - 1} \tag{1}$$

130 where ρ and GF are measured particle density (g cm^{-3}) and growth factor at t (min), respectively.

131 ρ_0 is the initial density of seed particles. The uncertainty in the density measurements was

132 estimated to be ± 0.03 g cm^{-3}.

133 To measure the optical properties of exposed particles, a 1-slpm flow from the chamber

134 was diluted by 4-slpm N$_2$ and introduced into a commercial integrating nephelometer (TSI 3563)

135 and a home-built cavity ring-down spectrometer (CRDS) throughout the experiment. Light

136 scattering (b_{sca}) and extinction (b_{ext}) at 532 nm were determined by the nephelometer and CRDS,

137 respectively. The nephelometer was calibrated by comparing measured b_{sca} with b_{ext} from CRDS

138 when measuring ammonium sulfate particles with diameters of 100 nm, 150 nm, 200 nm, 250 nm,

139   and 300 nm. The absorption coefficient (b_{abs}) was determined from ($b_{ext} - b_{sca}$), and SSA was

140   calculated from b_{sca}/b_{ext}.

141   The ID-CIMS using the hydronium reagent ion (H_3O^+) was employed to analyze gaseous

142   concentrations with a sample flow rate of 0.5 slpm from the chamber. The sample line was heated

143   to 70°C to reduce wall loss. Gas-phase concentrations of m-xylene and its oxidation products were

144   quantified by ID-CIMS. Briefly, the concentration of species A from the proton transfer reaction

145   ($H_3O^+ + A \rightarrow H_2O + HA^+$) is determined by,

$$[A] = \frac{S_A}{k_{PTR} \times \Delta t \times S_{RI}} \qquad (2)$$

146   where S_A and S_{RI} are the mass spectrum intensities for A and reagent ions, respectively. k_{PTR} is the

147   proton-transfer rate constant between A and H_3O^+ (Zhao and Zhang, 2004). $\Delta t = \frac{l}{U_i}$ is the retention

148   time of ions, which is determined by the length of the drift tube $l = 8$ cm and the ion drift velocity

149   U_i. The ion drift velocity U_i is determined from:

$$U_i = u_0 (\frac{760 \; torr}{p})(\frac{T}{273 \; K})E \qquad (3)$$

150   where $u_0 = 2$ cm^2 V^{-1} s^{-1} is the reduced ionic mobility (Dotan et al., 1976), $p = 3.0$ torr, $T = 298$ K,

151   and $E = 133$ V cm^{-1} is the voltage gradient in the drift tube. Alternatively, the concentrations of m-

152   xylene, dicarbonyls, and organic acids were also calibrated by preparing the vapors of m-xylene,

153   methylglyoxal with known mixing ratios in N_2, and using a permeation tube of propanoic acid,

154   respectively (Li et al., 2021a). The detection limit (defined as 3 times of the ratio of signal to noise)

155   for the oxidation products from m-xylene-OH reactions was estimated to be 50 ppt by the ID-

156   CIMS.

157   The steady-state OH concentration was determined by exponential fitting ($y = ke^{-bx}$) of

158   the decay of m-xylene concentration (Fig. 1a),

$$[\text{OH}] = \frac{b}{k_1} \tag{4}$$

where $k_1 = 2.4 \times 10^{-11}$ cm^3 molecule^{-1} s^{-1} is the second-order rate constant for m-xylene-OH

oxidation (Fan and Zhang, 2008). The estimated concentration of OH was 2.1×10^6 molecules cm^{-3} in our experiments.

We also estimated loss of condensable vapors to the chamber wall using the first-order

wall-loss coefficient, kw (s^{-1}), by considering gas-phase transport within the chamber (Zhang et

al., 2014)

$$kw = \left(\frac{A}{V}\right) \frac{\alpha_w \bar{c}}{4 + \frac{\pi}{2}\left(\frac{\alpha_w \bar{c}}{\sqrt{k_e D_g}}\right)} \tag{5}$$

where A/V is the surface to volume ratio of the chamber (equal to 6/L for a square chamber, where

$L = 1$ m is its dimension), α_w is the mass accommodation coefficient of vapors onto Teflon chamber

walls, $\bar{c}$ is the mean thermal speed of the molecules, k_e is the coefficient of eddy diffusion, which

is estimated to be 0.5 based on the loss rate of particles (McMurry and Rader, 1985),

$$k_e = \frac{(\frac{\pi L \beta_0}{12})^2}{D_b} \tag{6}$$

where β_0 is the fractional loss rate of particles,

$$\beta_0 = \frac{\Delta N}{N \times \Delta t} = \frac{15000 \text{ cm}^{-3} - 7500 \text{ cm}^{-3}}{15000 \text{ cm}^{-3} \times 7200 \text{ s}} = 1.4 \times 10^{-5} \text{ s}^{-1} \tag{7}$$

where N is the particle number concentration, $D_b = 6.75 \times 10^{-10}$ m^2 s^{-1} is the Brownian diffusion

coefficient for particles. D_g is the gas-phase diffusion coefficient. For NH$_3$, the mass

accommodation coefficient of vapors onto the chamber wall is 0.05 (Zhang et al., 2014). Gas-

phase diffusion constant D_g is 1.98×10^{-5} m^2 s^{-1}. The mean thermal speed $\bar{c}$ is 603 m s^{-1}. The first-

order wall-loss coefficient of NH$_3$ was calculated to be 1.2×10^{-2} s^{-1}.

175   The average concentration of NH_3 or NO_x (noted as X) is estimated by,

$$\overline{[X]} = \frac{(1 - e^{-k_w \times \Delta t_i})}{k_w \times \Delta t_i}[X]_0 \tag{8}$$

176   For initial injection of 400 ppb NH_3, the average concentration of NH_3 was estimated to be 19 ppb.

177   The first-order wall-loss rate of NO_x was measured to be $2.5 \times 10^{-3}\,h^{-1}$, leading to negligible wall-

178   loss (Qi et al., 2020).

179   The particle-phase chemical composition was analyzed by thermal desorption (TD) - ID -

180   CIMS (TD-ID-CIMS) (Wang et al., 2010). Seed particles after 20 min of exposure to

181   photooxidation were collected for 2 hours by a platinum filament (with a collection voltage of

182   about 3000 V) in a 2.5 slpm flow from the reaction chamber, and the analytes were evaporated by

183   heating the filament to 350°C for 2 s and detected by ID-CIMS using H_3O^+ as the reagent ions.

184   The mass resolution of TD-ID-CIMS was about 0.5 amu. The desorption signal was represented

185   by the relative intensity (RI) of the integrated peak area during heating. The uncertainties of TD-

186   ID-CIMS measurements arose from the flow rate, voltage, collection time, evaporation voltage,

187   and mass spectrometer ionization/detection efficiencies during particle collection and were

188   represented by the standard deviation of three repeated measurements. In both ID-CIMS and TD-

189   ID-CIMS configurations, an ion drift- tube was used. An electric field of E/N = 138 Td was applied

190   for ID-CIMS at high RH (i.e., 70%), and E/N = 110 Td was used for TD-ID-CIMS at low RH (<

191   1%). Formation of cluster ions was effectively suppressed, since a uniform electrical field in the

192   drift tube decomposed weakly-bonded cluster ions. Fragmentation using ID-CIMS or TD-ID-

193   CIMS was minimal, and all gaseous and particle-phase products were detected at their respective

194   parent-peaks, indicating little dissociation effect from either thermal desorption or ionization by

195   H_3O^+ (Yuan et al., 2017). For example, plausible fragment-ion peaks for oligomers and organic

196   acids are the monomeric ion-peaks and $[M-17]^+/[M-45]^+$ from α-cleavage, respectively. From our

197   detected particle-phase products (Fig. 2c), non-fragmental oligomers/NCO and organic acids

198   represented the dominant peaks, while negligible monomer (e.g., m/z = 73) and fragments for

199   organic acids (e.g., [M-17] or [M-45]) were detected, confirming little fragmentation by TD-ID-

200   CIMS measurement. Also, the major acetal/hemiacetal oligomers detected by TD-ID-CIMS at

201   high RH from m-xylene oxidation were consistent with a previous study showing intact oligomers

202   with thermal desorption (Claflin and Ziemann, 2019).

203   While the gaseous concentrations of the oxidation products, GF, SSA, and density were

204   temporally resolved in our experiments, the particle chemical composition reflected an overall

205   aerosol chemical makeup during an experiment. To assess the effects of different seed particles,

206   RH, and NH$_3$ on SOA and BrC formation, we compared the measured GF and SSA values after

207   120-min exposure to the m-xylene-OH oxidation.

208   **2.3 Uptake coefficient (γ) determination**

209   The uptake coefficient (γ) for COOs is calculated by,

$$\gamma = \frac{4 \times FR \times kp}{\bar{c} \times S} \tag{9}$$

210   where FR is the percent contributions of the COO species from m-xylene-OH oxidation to the

211   particle-phase mass intensity measured by TD-ID-CIMS. kp is measured first-order particle uptake

212   rate constant for COOs (i.e., glyoxal, methylglyoxal, γ-dicarbonyls, organic acids, PAQ, and

213   nitrophenols), which is calculated from the measured growth rate of seed particles,

$$kp = \frac{\pi \times \left(D_p^3 - D_0^3\right) \times \rho \times \bar{N} \times N_A}{6 \times MW \times [A] \times \Delta t} \tag{10}$$

214   where D_p and D_0 are the final and initial diameters of the particles during the time-period of 120

215   min, respectively, ρ is the density of total SOA, $\bar{N}$ = 11250 cm^{-3} is the average particle number

216   concentration during 120 min, Δt = 120 min is the exposure time, N$_A$ is Avogadro constant, MW

217   is the molar weight of species A, and [A] is the average gas phase concentration of species A. $\bar{c}$ is

218   the mean thermal speed of A. S is the average surface area of aerosols (cm^2 surface/cm^3 air) during

219   the period of $\Delta t = 120$ min,

$$S = \frac{\pi \int_{t=0}^{120\ min} D^2 \times HGf^2 \times \bar{N}dt}{\Delta t} \tag{11}$$

220   where D is the time-dependent particle diameter, *HGf* is the hygroscopic growth factor of particles

221   (Seinfeld and Pandis, 2016). The error bars of reactive coefficients are derived from the

222   propagation of uncertainties for the parameters in eqs. 9-11 (i.e., 1 σ of at least three repeated

223   measurements for each parameter).

224   **2.4   Simulation of gaseous oxidation products**

225   The gas-phase concentration of *m*-xylene-OH oxidation products were simulated by a tri-

226   exponential kinetic model to account for the gas-phase oxidation, chamber wall loss, and particle

227   uptake. The precursor A with an initial concentration of $[A]_0$ undergoes multiple steps of oxidation

228   to yield multi-generation products, P_n (where $n = 1, 2, 3, \dots$). Once formed, each product engages

229   in further oxidation with a pseudo first-order rate constant of $k_{n+1}' = k_{n+1}[OH]_{ss}$, particle uptake

230   with a rate constant of kp_n, and wall loss with a rate of kw_n. The forward rate constants, k_{n+1}, were

231   taken from MCM 3.3.1 (Jenkin et al., 2003). The rate constant of uptake kp_n is expressed by,

$$kp_n = \frac{1}{4}\gamma_n \bar{c} S \tag{12}$$

232   and the first-order wall loss rate constants were estimated by eq. 5 with the mass accommodation

233   coefficients α_w constrained by the measured time-dependent concentration. The gas-phase

234   concentrations of P_1 to P_3 are calculated by,

$$[P_1] = \frac{k_1'[A]_0}{k_2' + kw_1 + kp_1 - k_1'}(e^{-k_1't} - e^{-(k_2'+kw_1+kp_1)t}) \tag{13}$$

$$[P_2] = C_1 e^{-(k_3' + kw_2 + kp_2)t} + C_2 e^{-k_1' t} - C_3 e^{-(k_2' + kw_1 + kp_1)t} \tag{14}$$

$$[P_3] = C_4 e^{-(k_4' + kw_3 + kp_3)t} + C_5 e^{-(k_3' + kw_2 + kp_2)t} + C_6 e^{-k_1' t} - C_7 e^{-(k_2' + kw_1 + kp_1)t} \tag{15}$$

where C_1 to C_7 are constants, and k'_n denotes the pseudo-first order rate constant,

$$k'_n = k_n[\text{OH}] \tag{16}$$

The rate constants and values for C_1 to C_7 are summarized in Table S1.

2.5 COO yield

The COO yield (Y_{COO}) from *m*-xylene oxidation is determined from,

$$Y_{\text{COO}} = [\text{COO}_i]/\Delta[\text{C}_6\text{H}_4(\text{CH}_3)_2] \tag{17}$$

where i represents the type of COO species, and $\Delta[\text{C}_6\text{H}_4(\text{CH}_3)_2]$ denotes the concentration of *m*-xylene consumed due to OH oxidation. There were four types of COOs identified from our experiments, i.e., dicarbonyls for $i = 1$, carboxylic acids for $i = 2$, PAQ for $i = 3$, and nitrophenols for $i = 4$. The measured gaseous concentration for each COO is corrected for wall-loss and unreacted earlier generation products,

$$[\text{COO}_i] = \{[\text{COO}_{i,f}] + (\frac{1}{4}\gamma_i \bar{c} S + kw_i)\overline{[\text{COO}_i]}\Delta t\}/(1 - \frac{[A_f]}{[A_t]}) \tag{18}$$

where $[\text{COO}_{i,f}]$ and $\overline{[\text{COO}_i]}$ are the final and time-averaged gas-phase concentrations of COO$_i$ at 120 min, respectively. $[A_f]$ and $[A_t]$ are the unreacted and the total production of the earlier generation species A, respectively.

2.6 SOA mass concentration and yield

The measured SOA mass concentration is calculated based on the aerosol size growth and density,

$$M_{\text{SOA,meas.}} = \frac{1}{6}\pi(D_p^3 \times \rho_t - D_0^3 \times \rho_0) \times \bar{N} \tag{19}$$

251 where ρ_t and ρ_0 are the final and initial particle density during 120 min, respectively.

252 Alternatively, by categorizing COOs in accordance with the functional groups, we established a

253 framework to predict SOA formation from the measured production and reactivity. The SOA mass

254 concentration (M_{SOA}) is predicted from the measured uptake coefficients and average gas-phase

255 concentrations of COOs,

$$M_{SOA} = \sum_i^4 \frac{1}{4} \gamma_i \bar{c}_i S [A_i] MW_i \tag{20}$$

256 where MW_i is the molar weight of species i. γ_i is averaged over all identified species for each type

257 (i) of COOs, and $[A_i]$ is the sum of the measured concentrations of all identified species for type i

258 (time-averaged). The SOA mass yield is expressed by,

$$Y_{SOA} = M_{SOA} / \{\Delta[C_6H_4(CH_3)_2] \times MW_m\} \tag{21}$$

260 where MW_m is the molar weight of m-xylene.

261 To compare the measured and predicted SOA formation at RH = 10% and 70%, we

262 corrected the increased vapor wall loss and reduced particle surface area at RH = 70% compared

263 to 10% RH. A correction factor is determined from the average measured gas concentration ratios

264 (R_c) between 10% and 70% RH for each type of COOs. Additionally, a hygroscopic volume

265 enhancement factor (HVE) of 1.2 between 10% and 70% RH is adopted. The RH-corrected SOA

266 mass for each COO is estimated by,

$$M_{i,corr} = R_c \times M_{SOA} \times \frac{S_1}{S_2} \times \text{HVE} \tag{22}$$

267 where S_1 and S_2 are the particle surface areas at 10% and 70% RH, respectively.

268 **3.   Results and Discussions**

269 **3.1   Evolution of oxidation products**

270   To elucidate the production of COOs, we measured time-dependent gaseous concentrations

271   of m-xylene oxidation products. The OH-m-xylene reactions occur via dominantly OH-addition to

272   the aromatic ring to yield m-xylene-OH adducts and minorly H-abstraction from the methyl group

273   to form methylbenzyl radicals (about 4%) (Fan and Zhang, 2008). The m-xylene-OH adducts then

274   react with O_2 to form dimethylphenol via H-extraction or OH-m-xylene-O_2 peroxy radicals (RO_2)

275   via O_2 addition (Fig. S2a). While the m-xylene mixing ratio exhibits an exponential decay

276   throughout the experiments (Fig. 1a), the formation of the gas-phase oxidation products follows

277   the rate-determining steps involving successive OH-oxidation with three major generations (Fig.

278   1b-e). The first-generation products (P_1) include dimeththylphenol (m/z = 123) and

279   methylbenzaldehyde (m/z = 121), corresponding to OH addition to the aromatic ring (~96%) and

280   hydrogen extraction (~4%) from the methyl group, respectively (Fan and Zhang, 2008; Li et al.,

281   2021b). The second-generation products (P_2) mainly consist of methylglyoxal (m/z = 73),

282   methylbutenedial (m/z = 99), toluic acid (m/z = 137), and dimethylresorcinol (Fig. 1f and Fig. S2b),

283   which are produced from the P_1 reactions with OH/HO_2. For example, methylglyoxal and

284   methylbutenedial are formed from OH oxidation of dimeththylphenol and subsequent ring-

285   opening or from the primary peroxy radical. The latter undergoes cyclization to form the bicyclic

286   radical, which then reacts with O_2 to form the secondary peroxy radical, followed by reactions

287   with HO_2 and subsequent ring-cleavage (Fan and Zhang, 2008). The third-generation products (P_3)

288   contain mainly multi-functional organic acids, including pyruvic acid (m/z = 89), 4-oxo-2-

289   pentenoic acid (m/z = 115), and 3-methyl-4-oxo-2-pentenoic acid (m/z = 129) produced from the

290   subsequent reactions of dicarbonyls with OH. Note that P_n in Fig. 1b denotes the lumped product

291   of the nth generation, which is related the sequence of OH addition for m-xylene oxidation and

292   accounts for the various species detected by ID-CIMS (Fig. S2b).

293   The P_1 concentrations rise immediately upon initiating photooxidation and reach the peak

294   mixing ratios of about 20 ppb for dimeththylphenol and 9 ppb for methylbenzaldehyde. There is a

295   slight decline in P_1 concentrations after 70 to 100 mins, reflecting their consumption from further

296   OH oxidation (Fig. 1c). The P_2 concentrations follow those of P_1 (Fig. 1d and Fig. S3a) and reach

297   the peak mixing ratios ranging from 0.4 to 2.4 ppb, dependent on their subsequent oxidation by

298   OH as well as loss to the chamber wall and aerosols. Note that the concentration of toluic acid

299   rises later than those of the dicarbonyls, attributable to the slower rates for H-abstraction by OH

300   from the methyl group than OH-addition to the aromatic ring (Fan and Zhang, 2008). The P_3

301   concentrations increase monotonically after a delay of 10-20 mins and reach a mixing ratio from

302   sub-ppb to 2.5 ppb at 120 min (Fig. 1e and Fig. S3b). The initial concentration of m-xylene (e.g.,

303   1940 ppb) in our experiment is higher than that in the atmosphere, potentially inducing self- and

304   cross-reactions of RO_2 to form alkoxy radicals (RO) or dialkyl peroxides (ROOR') leading to

305   HOMs. However, negligible products relevant to HOMs were detected in our experiments,

306   indicating a minor importance for the self- and cross-reactions of RO_2 compared to the competing

307   reactions between RO_2 and $HO_2/NO/RO_2$ to form ring-opening products. Our results for

308   insignificant contribution of HOMs to SOA formation from m-xylene oxidation are consistent with

309   a small yield of HOMs reported in a previous study (Molteni et al., 2018).

310   We simulated the time-dependent evolution of the gaseous products by employing a tri-

311   exponential kinetic model (Fig. 1b and Table S1). Multi-generation oxidation of m-xylene occurs

312   via consecutive reaction steps to produce a multi-generation product, P_n (where n denotes the

313   sequence of OH oxidation), which subsequently engages in additional OH oxidation, wall loss,

314   and aerosol loss. Fig. 1b-d indicates that the simulated concentrations well reproduce those

315   measured for P_1 to P_3 by adopting our measured γ (to be discussed below) and estimated wall loss

316   rates (see Methods and Table S1 in SI).

317   **3.2   Particle size growth, SSA, and chemical speciation**

318   To evaluate SOA and BrC formation from COOs, we measured the time-dependent GF,

319   SSA, and density, after $(NH_4)_2SO_4$ seed particles are exposed to the *m*-xylene oxidation products

320   in the presence of 19 ppb NH_3 and at 70% RH (Fig. 2a-c, Exp. 1). The GF increases monotonically

321   and reaches a value of (2.41 ± 0.03) at 120 min (Fig. 2a), while the SSA declines steadily

322   throughout the exposure and reaches the value of (0.91 ± 0.01) at 120 min (Fig. 2b). The latter is

323   indicative of the production of light-absorbing BrC. The measured SSA for *m*-xylene is lower than

324   that previously reported for toluene under comparable experimental conditions (Li et al., 2021b).

325   The difference in SSA/BrC formation between toluene and *m*-xylene is explained by a higher yield

326   of methylglyoxal from *m*-xylene than from toluene (Jenkin et al., 2003; Nishino et al., 2010), since

327   methylglyoxal produces BrC more efficiently via aqueous reaction than glyoxal (Li et al., 2021a).

328   Analysis of particle chemical composition using TD-ID-CIMS reveals high abundances of

329   oligomers, nitrogen-containing organics (NCO) consisting of N-heterocycles/N-heterochains,

330   carboxylates, along with a small amount of dimethylresorcinol/benzoquinone (Fig. 2c). The

331   identified mass peaks are summarized in Tables S2 to S4. Assuming similar sensitivity to proton-

332   transfer reactions for the aerosol-phase organics, i.e., with the proton transfer reaction rate

333   constants of $(2 \text{ to } 4) \times 10^{-9}$ cm^3 molecule^{-1} s^{-1} (Zhao and Zhang, 2004), the contributions of

334   oligomers, NCO, carboxylates, and dimethylresorcinol/benzoquinone to the total SOA formation

335   are estimated to be 22%, 23%, 47%, and 8%, respectively, at 70% RH (Table S5). Note that the

336   TD-ID-CIMS method preserves the identify for all organic species without fragmentation,

337   providing unambiguous chemical speciation for the aerosol-phase products.

338   **3.3   Effects of seed particles, NH$_3$, RH, and NO$_x$**

339   We assessed the dependence of SOA/BrC formation from *m*-xylene-OH oxidation on

340   different seed particles (Exp. 1-4), NH$_3$ concentration (Exp. 1-12), RH (Exp. 1,13-15), and NO$_x$

341   concentration (Exp. 1,16-18). Fig. 3a shows that (NH$_4$)$_2$SO$_4$ in the presence of 19 ppb NH$_3$ exhibits

342   the largest GF and lowest SSA at 120 min, which are explained by the chemical mechanisms

343   leading to the formation of the observed aerosol-phase products. While dicarbonyls undergo

344   aqueous phase reactions to form oligomers (Fig. S4) (Ji et al., 2020; Li et al., 2021a), organic acids

345   engage in ionic dissociation and acid-base reaction to yield carboxylates (Fig. 3b). In addition, the

346   reaction of dicarbonyls with NH$_3$ produces N-heterocycles/N-heterochains (Fig. S5), which are

347   light-absorbing (Marrero-Ortiz et al., 2019; Li et al., 2021a). Oligomerization of dicarbonyls

348   involves protonation, hydration, and deprotonation, which are mediated by carbenium ions via

349   nucleophilic addition (Ji et al., 2020; Li et al., 2021a). While protonation of dicarbonyls to yield

350   carbenium ions is promoted by hydrogen ion activity, high acidity hinders hydration and

351   deprotonation, explaining the largest GF and the smallest SSA on weakly acidic (NH$_4$)$_2$SO$_4$

352   particles in the presence NH$_3$ (Fig. 3a). In addition, uptake of dicarbonyls, organic acids, and PAQ

353   is likely facilitated on aqueous (NH$_4$)$_2$SO$_4$ particles, because of surface propensity of charge-

354   separation at the interface (Hua et al., 2011; Shi et al., 2020). Specifically, surface-abundant NH$_4^+$

355   cations arising from interfacial charge separation of (NH$_4$)$_2$SO$_4$ likely exert electrostatic attraction

356   to gaseous oxygenated species (with a negative charge character) to enhance uptake for

357   dicarbonyls, organic acids, and PAQ (Li et al., 2021a,b). The most efficient formation of SOA and

358   BrC on (NH$_4$)$_2$SO$_4$ particles in the presence of NH$_3$ are also consistent with the measured highest

359   intensities for oligomers and NCO (Fig. 3b). On the other hand, ionic dissociation and acid-base

360   reaction to yield carboxylates occur efficiently in the presence of NH$_3$/NaCl, as evident from the

361　increasing carboxylate intensity from NH_4HSO_4 to NaCl (Fig. 3b). The GF and SSA increase and

362　decrease, respectively, with NH_3 from 0 to 27 ppb for all three types of seed particles (Fig. 4a,b),

363　relevant to the reactions of NH_3 with dicarbonyls to form NCO and with organic acids to form

364　ammonium carboxylates. The analysis of the particle composition confirms that the intensities of

365　oligomers, NCO, and carboxylates increase with the NH_3 concentration (Fig. 4c-e).

366　　　We carried out additional experiments by varying RH from 10% to 70% in the presence of

367　19 ppb NH_3 (Fig. 5). The GF decreases with increasing RH from (3.10 ± 0.06) at RH = 10% to

368　(2.41 ± 0.03) at RH = 70% (Fig. 5a). The measured SSA at 120 min is close to unity at 10% and

369　30% RH and decreases with increasing RH (Fig. 5a), indicating negligible NCO formation at low

370　RH but significant NCO formation at RH above 50%. Carboxylates represent the dominant

371　constituent throughout the RH range (i.e., 85% at 10% RH to 47% at 70% RH), while the

372　contributions of oligomers and NCO are small at low RH (2-5% at RH < 40%) and become

373　increasingly significant at high RH (15-23% at RH > 50%) (Fig. 5b). The fraction for PAQ (8%)

374　is nearly invariant with RH. For $(NH_4)_2SO_4$ particles, the deliquescent and efflorescent points are

375　at 80% and 36% RH, respectively (Li et al., 2021b). At low RH (10% and 30%), aqueous reactions

376　to yield oligomers/NCO are minimal because of small water activity and significantly suppressed

377　protonation and oligomerization. On the other hand, carboxylic acids readily undergo ionic

378　dissociation or acid-base reaction, since organic acids efficiently retain water even at low RH (Xue,

379　2009). The equilibrium vapor pressures for PAQ are much lower than those for organic acids

380　(Table S6), facilitating more efficient condensation. Additionally, wall-loss of COOs is more

381　pronounced at high RH (Li et al., 2021b), explaining the decreased GF with increasing RH.

382　Measurement of gaseous concentrations for COOs shows that wall-loss is 1.5 to 4.6 times more

383   efficient at 70% RH than at 10% RH, while wall loss of *m*-xylene is negligible at both RH levels

384   (Table S7).

385   We determined the total density and the density of the SOA fraction for $(NH_4)_2SO_4$ seed

386   particles exposed to *m*-xylene oxidation (Fig. 5 c,d). The measured densities are distinct between

387   10 and 70% RH. At 10% RH, the total density decreases monotonically, while the SOA density

388   increases slightly with reaction time, i.e., from 1.27 to 1.39 g cm^{-3} (Fig. 5c), indicating minor

389   oligomers and dominant carboxylic acids at low RH. At 70% RH, the total particle density initially

390   decreases from 1.77 g cm^{-3} to 1.41 g cm^{-3} (at a GF of 1.24) and subsequently increases steadily to

391   1.56 g cm^{-3} at 120 min. The SOA density on $(NH_4)_2SO_4$ particles increases from 1.26 g cm^{-3} at 10

392   min to 1.55 g cm^{-3} at 120 min (Fig. 5d). The evolution in the densities reflects the variation in the

393   chemical composition. The initial particle growth is dominated by small oligomers, imidazoles

394   from methylglyoxal/methylbutenedial, and early-generation organic acids (e.g., toluic acid), with

395   the densities from 0.98 to 1.27 g cm^{-3} (Table S8). Subsequent particle growth from

396   methylglyoxal/methylbutenedial yields large oligomers, with the densities of 1.71-1.90 g cm^{-3}

397   (Table S8).

398   To evaluate the NO$_x$ effects, we performed experiments on $(NH_4)_2SO_4$ seed particles by

399   varying the initial NO$_x$ concentration from 0 to 500 ppb (Fig. 6). Three major nitrophenols are

400   identified from NO$_2$ addition to the OH-*m*-xylene adduct, i.e., 4-methyl-2-nitrophenol ($m/z = 154$),

401   dimethyl nitrophenol ($m/z = 168$), and dimethyl-4-nitrocatechol ($m/z = 184$) (Fig. 6a). The

402   production of nitrophenols is much smaller than those for dicarbonyls and organic acids, consistent

403   with a smaller yield (less than 7%) for nitrophenols (Fan and Zhang, 2008). The GF on $(NH_4)_2SO_4$

404   seed particles with NH$_3$ decreases from 2.41 ± 0.03 to 2.18 ± 0.03 with 0 to 500 ppb NO$_x$ (Fig. 6b).

405   The SSA decreases significantly from 0.911 ± 0.006 to 0.839 ± 0.003 with increasing NO$_x$ (Fig.

406   6b), because of the formation of light-absorbing nitrophenols (Hems and Abbatt, 2018; Li et al.,

407   2021b). Analysis of particle composition reveals that the decreasing GF with increasing NO_x

408   correlates with simultaneous decreases of carboxylates, oligomers, and NCOs and with increasing

409   nitrophenols in the aerosol-phase (Fig. 6c). Overall, nitrophenols contribute 2% to 4% to the SOA

410   formation. Addition of NO_x not only produces nitrophenols and but also alters the cycling between

411   RO_2 and alkoxy (RO) radicals, leading to re-distributions of COOs. The presence of NO_x decreases

412   dicarbonyls and organic acids, as evident from decreased intensities for oligomers, NCO, and

413   carboxylates in the aerosol-phase with increasing NO_x (Fig. 2h).

414   **3.4   COO and SOA Yields**

415   From the measured GF and COO concentrations, we derived the γ, which is widely

416   employed to represent aerosol formation in atmospheric models (Zhang et al., 2015). The

417   measured γ varies with the functionality of COOs and RH on $(NH_4)_2SO_4$ seed particles (Fig. 7a).

418   Results of the γ values for COOs are also summarized in Table S9. The γ for dicarbonyls is the

419   highest (from 3×10^{-3} to 1.3×10^{-2}) at 70% RH but is significantly reduced (from 3.7×10^{-4} to 1.0

420    $\times 10^{-3}$) at 10% RH, while the γ's for organic acids, PAQ, and nitrophenols are slightly higher at

421   70% RH. Among the organic acids, the γ correlates with the acid dissociation constant and

422   solubility, which are the highest for pyruvic acid and the lowest for toluic acid. The standard

423   variation in γ (within one σ) among each COO type is within 50%, 40%, 30%, and 15% for

424   dicarbonyls, organic acids, PAQ, and nitrophenols, respectively. From the measured

425   concentrations of COOs and m-xylene, we determined the COO yields (Y_{COO}) using eq. 17, by

426   considering four COO species, i.e., dicarbonyls for $i = 1$, carboxylic acids for $i = 2$, PAQ for $i = 3$,

427   and nitrophenols for $i = 4$ (Table S7). The Y_{COO} values for dicarbonyls, organic acids, PAQ, and

428   nitrophenols are 25%, 37%, 5%, and 3%, respectively (Fig. 7b), indicating significant production

429   of COOs from *m*-xylene oxidation.

430   Our work shows significant increase in particle size (Fig. 2a) and constantly varying

431   particle properties, i.e., SSA (Fig. 2b) and density (Fig. 5c,d), which correlate closely with the

432   gaseous COO production (Fig. 1). These results imply a highly nonequilibrium kinetic process

433   leading to SOA formation from m-xylene oxidation, which cannot be described by equilibrium

434   partitioning. The gas-to-particle conversion from *m*-xylene oxidation is dominated by several

435   volatile COO species (i.e., organic acids and dicarbonyls) and with minor contribution from

436   condensation of low-volatility COO (i.e., polyhydroxy aromatics/quinones, and nitrophenols) (Fig.

437   5b). In our study, the vapor pressures of the detected gaseous oxidation products for organic acids

438   and dicarbonyls are too large to explain the measured particle growth via equilibrium partitioning

439   (Table S6). Specifically, the saturation vapor pressures of organic acids detected in the particle-

440   phase range from 1.9×10^{-3} to 6.6×10^{-6} atm, while their gas-phase concentrations range from 0.5

441   to 2.5 ppb. Similarly, the saturation vapor pressures of dicarbonyls detected in the particle-phase

442   range from 1.6×10^{-1} to 3.9×10^{-4} atm, while their gas-phase concentrations range from 0.5 to 2.2

443   ppb. The high saturation vapor pressures and low gas-phase concentrations for dicarbonyls and

444   organic acids render equilibrium partitioning implausible for these COOs in our experiments. Also,

445   the detection of the particle-phase products confirms that organic acids and dicarbonyls directly

446   participate in heterogeneous reactions to yield low-volatile products. Moreover, volatility-based

447   equilibrium partitioning cannot not explain the variations in the particle size growth, SSA, and

448   chemical compositions on different seed particles (Fig. 3). Clearly, the gas-to-particle conversion

449   from *m*-xylene oxidation likely involves several distinct heterogeneous processes, including the

450   interfacial interaction, ionic dissociation/acid-base reaction, and nucleophilic oligomerization (Li

451   et al., 2021a,b).

452   We establish a functionality-based SOA formation to predict the aerosol mass

453   concentration (M_{SOA}) from the gaseous concentrations and γ's for COOs using eq. 20. The M_{SOA}

454   is calculated from the measurements of the averaged γ (Fig. 7a and Table S10) and the time-

455   averaged concentrations for each COO type (Table S7). While the production of COOs is

456   dependent on the VOC types and photooxidation, the aerosol-phase reactivity of COOs, as

457   represented by γ, is dependent on the functionality for a given aerosol type. Thus, SOA formation

458   from various VOC types can be predicted from the production and reactivity for COOs based on

459   the experimental measurements, by categorizing COOs in accordance with their functional groups.

460   The overall gas uptake onto liquid or solid particles is commonly described by an empirical

461   framework on the basis of an effective γ, which accounts for the gas-phase diffusion, the interfacial

462   process (i.e., accommodation), and the aerosol-phase processes (Zhang et al., 1994; Ravishankara,

463   1997). The aerosol-phase processes include thermodynamically driven surface or volume-limited

464   partitioning (including condensation for low-volatile species or solubility for volatile species) and

465   chemically driven reactivity relevant to the functionality (Gomez et al., 2015). Ultimately, the

466   SOA growth is dependent on the volatility of the aerosol-phase products. Evidently, there are two

467   pathways to produce low-volatile compounds, i.e., gas-phase oxidation to yield low-volatile COOs

468   that subsequently under condensation and multiphase reactions of volatile COOs to form low-

469   volatile products in the aerosol-phase. In our study, the gas-to-particle conversion from *m*-xylene

470   oxidation occurs dominantly via the latter, i.e., reactive uptake for di-carbonyls and organic acids,

471   with a relatively small contribution from the former, i.e., condensation by low-volatile PAQs and

472   nitrophenols. Also, our measured uptake coefficient for each COO type (γ_i) is derived from the

473 measured particle growth (eqs. 9 and 10), which implicitly accounts for non-continuum diffusion,

474 imperfect accommodation, and evaporation.

475   To assess the consistency of our approach, we compared the predicted and measured SOA

476 mass yields (Y_{SOA}), according to eq. 21. The predicted Y_{SOA} is $(11 \pm 3)\%$ and $(6 \pm 1)\%$,

477 respectively, at 10% and 70 % RH, comparable to the measured values of $(14 \pm 0.4)\%$ and $(6.3 \pm$

478 $0.2)\%$ on $(NH_4)_2SO_4$ seed particles (Fig. 7c). The slight differences between the predicted and

479 measured Y_{SOA}'s are explainable by the uncertainties related to lumping each COO type (i.e.,

480 averaging the γ values) as well as unaccounted low-abundant COO species. To account for the

481 RH-dependent wall loss for COOs, we corrected Y_{SOA} from the measured gaseous concentrations

482 at varying RH (see Methods and Table S7). Such correction results in an increase of about one to

483 four times for Y_{SOA} at 10% and 70% RH, yielding the values of $(20 \pm 4)\%$ and $(32 \pm 7)\%$,

484 respectively (Fig. 7c). Under atmospheric conditions, SOA/BrC formation from *m*-xylene is

485 expected to be enhanced at high RH, because of significantly enhanced aqueous reaction, larger

486 aerosol surface-area, and higher water activity. Field measurements showed significantly enhanced

487 SOA formation with increasing RH during severe haze evolution (Guo et al., 2014; Peng et al.,

488 2021).

489 **4.   Conclusions**

490   In this work we have elucidated the production of COOs and their roles in SOA formation

491 from *m*-xylene oxidation. The major advantages of our analytical methodologies lie in

492 simultaneous monitoring of the evolutions of gaseous oxidation products and aerosol properties

493 when seed particles are exposed to the oxidation products, which allows for assessment of multi-

494 generation production of SOA and BrC. Also, our experimental approach remedies the deficiency

495 of wall loss of reactive gaseous and particles, which represents a main obstacle in experimental

496   investigation using environmental chambers (Zhang et al., 2014; Huang et al., 2018). OH-initiated

497   oxidation of *m*-xylene produces four distinct COO types consisting of dicarbonyls, carboxylic

498   acids, polyhydroxy aromatics/quinones, and nitrophenols from early-generation (P_2 and P_3), with

499   the yields of 25%, 37%, 5%, and 3%, respectively. SOA formation occurs via several

500   heterogeneous processes, including interfacial interaction, ionic dissociation/acid-base reaction,

501   and oligomerization, with the yields of $(20 \pm 4)\%$ at 10% RH and $(32 \pm 7)\%$ at 70% RH. The

502   identified aerosol-phase products include dominant oligomers, N-heterocycles/N-heterochains,

503   and carboxylates at high RH and dominant carboxylates at low RH, along with small amounts of

504   PAQ and nitrophenols (in the presence of NO_x). The nitrogen-containing organics consisting of

505   N-heterocycles, N-heterochains, and nitrophenols are light-absorbing, characterized by low SSA.

506   The measured γ for COOs is dependent on the functionality, ranging from 3.7×10^{-4} to 1.3×10^{-2}.

507   A kinetic framework is developed to predict SOA formation from the concentration and γ for

508   COOs. Our results illustrate that SOA formation from *m*-xylene oxidation is accurately quantified

509   from the abundance and reactivity for COOs (i.e., eq. 20). Notably, this kinetic framework

510   accounts for the interfacial process (i.e., mass accommodation) as well as aqueous reactions (i.e.,

511   oligomerization and acid-base reactions) without the assumption of gas-particle equilibrium. We

512   envisage that this functionality-based approach is applicable to predict SOA formation from VOC

513   photooxidation using experiment/field measured or model-simulated COOs, aerosol surface area,

514   and reactivity. We conclude that photochemical oxidation of *m*-xylene represents a major source

515   for SOA and BrC formation under urban conditions, because of its large abundance, high reactivity

516   with OH, and high yields for COOs.

517   **ACKNOWLEDGEMENTS**

REFERENCES

Atkinson, R. Atmospheric Chemistry of VOCs and NO_x. Atmos. Environ., 34, 2063–2101, 2000.

Calvert, J. G., Atkinson, R., Becker, K. H., Kamens, R. M., Seinfeld, J. H., Wallington, T. H., and Yarwood, G.: The Mechanisms of Atmospheric Oxidation of Aromatic Hydrocarbons, Oxford University Press: New York., 2002.

Claflin, M. S. and Ziemann, P. J.: Thermal desorption behavior of hemiacetal, acetal, ether, and ester oligomers, Aerosol Sci. Technol., 53(4), 473–484, doi:10.1080/02786826.2019.1576853, 2019.

Dotan, I., Albritton, D. L., Lindinger, W. and Pahl, M.: Mobilities of $CO2+$, $N2H+$, $H3O+$, $H3O+\cdot H2O$, and $H3O+\cdot(H2O)2$ ions in N2, J. Chem. Phys., 65(11), 5028–5030, doi:10.1063/1.432943, 1976.

Fan, J., and Zhang, R.: Density Functional Theory Study on OH-Initiated Atmospheric Oxidation of m-Xylene, J. Phys. Chem. A, 112(18), 4314–4323, doi:10.1021/jp077648j, 2008.

Faust, J. A., Wong, J. P. S., Lee, A. K. Y., and Abbatt, J. P. D.: Role of Aerosol Liquid Water in Secondary Organic Aerosol Formation from Volatile Organic Compounds, Environ. Sci. Technol., 51, 1405− 1413, 2017.

Finlayson-Pitts, B. J., and Pitts, J. N.: Chemistry of the Upper and Lower Atmosphere: Theory, Experiments and Applications, Academic Press, San Diego, 2000.

Fortner, E. C., Zheng, J., Zhang, R., Berk Knighton, W., Volkamer, R. M., Sheehy, P., Molina, L., and André, M.: Measurements of Volatile Organic Compounds Using Proton Transfer Reaction – Mass Spectrometry during the MILAGRO 2006 Campaign, Atmos. Chem. Phys., 9(2), 467–481, doi:10.5194/acp-9-467-2009, 2009.

Fortner, E.C., Zhao, J., and Zhang, R.: Development of ion drift-chemical ionization mass spectrometry, Anal. Chem., 76, 5436-5440, 2004.

Fountoukis, C. and Nenes, A.: SORROPIA II: A Computationally Efficient Thermodynamic Equilibrium Model for K+–Ca2+–Mg2+–NH4+–Na+–SO42−–NO3−–Cl–H2O Aerosols., Atmos. Chem. Phys., 7(17), 4639–4659, doi:10.5194/acp-7-4639-2007, 2007.

Garmash, O., Rissanen, M. P., Pullinen, I., Schmitt, S., Kausiala, O., Tillmann, R., Zhao, D., Percival, C., Bannan, T. J., Priestley, M., Hallquist, Å. M., Kleist, E., Kiendler-Scharr, A., Hallquist, M., Berndt, T., McFiggans, G., Wildt, J., Mentel, T. F., and Ehn, M.: Multi-generation OH oxidation as a source for highly oxygenated organic molecules from aromatics, Atmos. Chem. Phys., 20(1), 515–537, doi:10.5194/acp-20-515-2020, 2020.

Gomez, M.E., Lin, Y., Guo, S., and Zhang, R.: Heterogeneous chemistry of glyoxal on acidic solutions – An oligomerization pathway for secondary organic aerosol formation, J. Phys. Chem., 118, 4457-4463, doi:10.1021/jp509916r, 2015.

Guo, S., Hu, M., Zamora, M. L., Peng, J., Shang, D., Zheng, J., Du, Z., Wu, Z., Shao, M., Zeng, L., Molina, M. J., and Zhang, R.: Elucidating severe urban haze formation in China, Proc. Natl. Acad. Sci. USA, 111(49), 17373–17378, doi:10.1073/pnas.1419604111, 2014.

Guo, S., Hu, M., Lin, Y., Gomez-Hernandez, M., Zamora, M. L., Peng, J., Collins, D. R., and Zhang, R.: OH-Initiated Oxidation of m-Xylene on Black Carbon Aging, Environ. Sci. Technol., 50(16), 8605–8612, doi:10.1021/acs.est.6b01272, 2016.

Guo, S., Hu, M., Peng, J., Wu, Z., Zamora, M. L., Shang, D., Du, Z., Zheng, J., Fang, X., Tang, R., Wu, Y., Zeng, L., Shuai, S., Zhang, W., Wang, Y., Ji, Y., Li, Y., Zhang, A. L., Wang, W., Zhang, F., Zhao, J., Gong, X., Wang, C., Molina, M. J. and Zhang, R.: Remarkable nucleation and growth of ultrafine particles from vehicular exhaust, Proc. Natl. Acad. Sci., 117(7), 3427–3432, doi:10.1073/pnas.1916366117, 2020.

De Haan, D. O., Hawkins, L. N., Kononenko, J. A., Turley, J. J., Corrigan, A. L., and Tolbert, M. A., Jimenez, J. L.: Formation of Nitrogen- Containing Oligomers by Methylglyoxal and Amines in Simulated Evaporating Cloud Droplets, Environ. Sci. Technol., 45, 984− 991, 2011.

De Haan, D. O., Hawkins, L. N., Welsh, H. G., Pednekar, R., Casar, J. R., Pennington, E. A., de Loera, A., Jimenez, N. G., Symons, M. A., Zauscher, M., Pajunoja, A., Caponi, L., Cazaunau, M., Formenti, P., Gratien, A., Pangui, E., and Doussin, J.-F.: Brown Carbon Production in Ammonium- or Amine-Containing Aerosol Particles by Reactive Uptake of Methylglyoxal and Photolytic Cloud Cycling, Environ. Sci. Technol., 51(13), 7458–7466, doi:10.1021/acs.est.7b00159, 2017.

Heald, C. L., Jacob, D. J., Park, R. J., Russell, L. M., Huebert, B. J., Seinfeld, J. H., Liao, H., and Weber, R. J.: A Large Organic Aerosol Source in the Free Troposphere Missing from Current Models. Geophys. Res. Lett., 32, 1−4, 2005.

Hems, R. F., and Abbatt, J. P. D.: Aqueous Phase Photo-oxidation of Brown Carbon Nitrophenols: Reaction Kinetics, Mechanism, and Evolution of Light Absorption, ACS Earth Sp. Chem., 2(3), 225–234, doi:10.1021/acsearthspacechem.7b00123, 2018.

Hodzic, A., Kasibhatla, P. S., Jo, D. S., Cappa, C. D., Jimenez, J. L., Madronich, S., and Park, R. J.: Rethinking the Global Secondary Organic Aerosol (SOA) Budget: Stronger Production, Faster Removal, Shorter Lifetime. Atmos. Chem. Phys., 16, 7917−7941, 2016.

Hua, W., Jubb, A. M., and Allen, H. C.: Electric Field Reversal of Na2SO4, (NH4)2SO4, and Na2CO3 Relative to CaCl2 and NaCl at the Air/Aqueous Interface Revealed by Heterodyne Detected Phase-Sensitive Sum Frequency, J. Phys. Chem. Lett., 2(20), 2515–2520, doi:10.1021/jz200888t, 2011.

Huang, Y., Zhao, R., Charan, S. M., Kenseth, C. M., Zhang, X., and Seinfeld, J. H.: Unified Theory of Vapor–Wall Mass Transport in Teflon-Walled Environmental Chambers, Environ. Sci. Technol., 52(4), 2134–2142, doi:10.1021/acs.est.7b05575, 2018.

Intergovernmental Panel on Climate Change (IPCC). *Climate Change 2013: The Physical Science Basis. Contribution of Working Group I to the Fifth Assessment Report of the Intergovernmental Panel on Climate Change*. Cambridge University Press, 2013.

Jenkin, M. E., Saunders, S. M., Wagner, V., and Pilling, M. J.: Protocol for the development of the Master Chemical Mechanism, MCM v3 (Part B): tropospheric degradation of aromatic volatile organic compounds, Atmos. Chem. Phys., 3(1), 181–193, doi:10.5194/acp-3-181-2003, 2003.

Ji, Y., Zhao, J., Terazono, H., Misawa, K., Levitt, N. P., Li, Y., Lin, Y., Peng, J., Wang, Y., Duan, L., Pan, B., Zhang, F., Feng, X., An, T., Marrero-Ortiz, W., Secrest, J., Zhang, A. L., Shibuya, K., Molina, M. J., and Zhang, R.: Reassessing the atmospheric oxidation mechanism of toluene, Proc. Natl. Acad. Sci. USA, 114(31), 8169–8174, doi:10.1073/pnas.1705463114, 2017.

Ji, Y., Shi, Q., Li, Y., An, T., Zheng, J., Peng, J., Gao, Y., Chen, J., Li, G., Wang, Y., Zhang, F., Zhang, A. L., Zhao, J., Molina, M. J., and Zhang, R.: Carbenium ion-mediated oligomerization of methylglyoxal for secondary organic aerosol formation, Proc. Natl. Acad. Sci. USA, 117(24), 13294 LP – 13299, doi:10.1073/pnas.1912235117, 2020.

Jia, L., and Xu, Y.: Effects of Relative Humidity on Ozone and Secondary Organic Aerosol Formation from the Photooxidation of Benzene and Ethylbenzene, Aerosol Sci. Technol., 48(1), 1–12, doi:10.1080/02786826.2013.847269, 2014.

Jia, L., and Xu, Y.: Different roles of water in secondary organic aerosol formation from toluene and isoprene, Atmos. Chem. Phys., 18(11), 8137–8154, doi:10.5194/acp-18-8137-2018, 2018.

Li, G., Zhang, R., Fan, J., and Tie, X.: Impacts of biogenic emissions on photochemical ozone production in Houston, Texas, J. Geophys. Res., 112, D10309, doi:10.1029/2006JD007924, 2007.

Li, Y., Ji, Y., Zhao, J., Wang, Y., Shi, Q., Peng, J., Wang, Y., Wang, C., Zhang, F., Wang, Y., Seinfeld, J. H., and Zhang, R.: Unexpected Oligomerization of Small α-Dicarbonyls for Secondary Organic Aerosol and Brown Carbon Formation, Environ. Sci. Technol., 55(8), 4430–4439, doi:10.1021/acs.est.0c08066, 2021a.

Li, Y., Zhao, J., Wang, Y., Seinfeld, J. H., and Zhang, R.: Multigeneration Production of Secondary Organic Aerosol from Toluene Photooxidation, Environ. Sci. Technol., 55, 8592−8603, doi:10.1021/acs.est.1c02026, 2021b.

Liu, J., Zhang, F., Xu, W., Sun, Y., Chen, L., Li, S., Ren, J., Hu, B., Wu, H., and Zhang, R.: Hygroscopicity of Organic Aerosols Linked to Formation Mechanisms, Geophys. Res. Lett., 48(4), e2020GL091683, doi:https://doi.org/10.1029/2020GL091683, 2021.

Marrero-Ortiz, W., Hu, M., Du, Z., Ji, Y., Wang, Y. Y., Guo, S., Lin, Y., Gomez-Hermandez, M., Peng, J., Li, Y., Secrest, J., Zamora, M. L., Wang, Y. Y., An, T., and Zhang, R.: Formation and

624 Optical Properties of Brown Carbon from Small α-Dicarbonyls and Amines, , 53(1), 117–126,
625 doi:10.1021/acs.est.8b03995, 2019.

626 McMurry, P. H. and Rader, D. J.: Aerosol Wall Losses in Electrically Charged Chambers, Aerosol
627 Sci. Technol., 4(3), 249–268, doi:10.1080/02786828508959054, 1985.

628 Molina, L. T.: Introductory lecture: air quality in megacities, Faraday Discuss, 226, 9-52,
629 10.1039/d0fd00123f, 2021.

630 Moise, T., Flores, J. M., and Rudich, Y.: Optical Properties of Secondary Organic Aerosols and
631 Their Changes by Chemical Processes, Chem. Rev., 115, 4400−4439, 2015.

632 Molteni, U., Bianchi, F., Klein, F., El Haddad, I., Frege, C., Rossi, M. J., Dommen, J., and
633 Baltensperger, U.: Formation of highly oxygenated organic molecules from aromatic compounds,
634 Atmos. Chem. Phys., 18(3), 1909–1921, doi:10.5194/acp-18-1909-2018, 2018.

635 National Academies of Sciences Engineering and Medicine (NASEM): The Future of Atmospheric
636 Chemistry Research: Remembering Yesterday, Understanding Today, Anticipating Tomorrow,
637 The National Academies Press, Washington, DC., 2016.

638 Ng, N. L., Kroll, J. H., Chan, A. W. H., Chhabra, P. S., Flagan, R. C., and Seinfeld, J. H.: Secondary
639 organic aerosol formation from m-xylene, toluene, and benzene, Atmos. Chem. Phys., 7(14),
640 3909–3922, doi:10.5194/acp-7-3909-2007, 2007.

641 Nishino, N., Arey, J., and Atkinson, R.: Formation Yields of Glyoxal and Methylglyoxal from the
642 Gas-Phase OH Radical-Initiated Reactions of Toluene, Xylenes, and Trimethylbenzenes as a
643 Function of NO2 Concentration, J. Phys. Chem. A, 114(37), 10140–10147,
644 doi:10.1021/jp105112h, 2010.

645 Peng, J., Hu, M., Shang, D., Wu, Z., Du, Z., Tan, T., Wang, Y., Zhang, F., and Zhang, R.:
646 Explosive secondary aerosol formation during severe haze in the North China Plain, Environ. Sci.
647 Technol., 55(4), 2189–2207, 2021.

648 Pope, C. A., III, Burnett, R. T., Thun, M. J., Calle, E. E., Krewski, D., Ito, K., and Thurston, G.
649 D.: Lung Cancer, Cardiopulmonary Mortality, and Long-Term Exposure to Fine Particulate Air
650 Pollution. J. Am. Med. Assoc., 287, 1132−1141, 2002.

651 Qi, X., Zhu, S., Zhu, C., Hu, J., Lou, S., Xu, L., Dong, J. and Cheng, P.: Smog chamber study of
652 the effects of NOx and NH3 on the formation of secondary organic aerosols and optical properties
653 from photo-oxidation of toluene, Sci. Total Environ., 727, 138632,
654 doi:https://doi.org/10.1016/j.scitotenv.2020.138632, 2020.

655 Ravishankara, A.R.: Heterogeneous and multiphase chemistry in the troposphere, Science 276,
656 1058-1065, 1997.

657 Schwantes, R. H., Schilling, K. A., McVay, R. C., Lignell, H., Coggon, M. M., Zhang, X.,
658 Wennberg, P. O., and Seinfeld, J. H.: Formation of highly oxygenated low-volatility products from
659 cresol oxidation, Atmos. Chem. Phys., 17(5), 3453–3474, doi:10.5194/acp-17-3453-2017, 2017.

Seinfeld, J. H., and Pandis, S. N.: Atmospheric chemistry and physics: from air pollution to climate change, John Wiley & Sons., 2016.

Shi, Q., Zhang, W., Ji, Y., Wang, J., Qin, D., Chen, J., Gao, Y., Li, G., and An, T.: Enhanced uptake of glyoxal at the acidic nanoparticle interface: implications for secondary organic aerosol formation, Environ. Sci. Nano, 7, 1126−1135, 2020.

Shrivastava, M., Cappa, C. D., Fan, J., Goldstein, A. H., Guenther, A. B., Jimenez, J. L., Kuang, C., Laskin, A., Martin, S. T., Ng, N. L., Petaja, T., Pierce, J. R., Rasch, P. J., Roldin, P., Seinfeld, J. H., Shilling, J., Smith, J. N., Thornton, J. A., Volkamer, R., Wang, J., Worsnop, D. R., Zaveri, R. A., Zelenyuk, A., and Zhang, Q.: Recent advances in understanding secondary organic aerosol: Implications for global climate forcing, Rev. Geophys., 55(2), 509–559, doi:10.1002/2016RG000540, 2017.

Song, C., Na, K., Warren, B., Malloy, Q., and Cocker, D. R.: Secondary Organic Aerosol Formation from m-Xylene in the Absence of NOx, Environ. Sci. Technol., 41(21), 7409–7416, doi:10.1021/es070429r, 2007.

Suh, I., Lei, W., and Zhang, R.: Experimental and theoretical studies of isoprene reaction with NO$_3$, J. Phys. Chem., 105, 6471-6478, 2001.

Tan, Y., Lim, Y. B., Altieri, K. E., Seitzinger, S. P., and Turpin, B. J.: Mechanisms leading to oligomers and SOA through aqueous photooxidation: insights from OH radical oxidation of acetic acid and methylglyoxal, Atmos. Chem. Phys., 11, 18319−18347, 2012.

Wang, G., Zhang, F., Peng, J., Duan, L., Ji, Y., Marrero-Ortiz, W., Wang, J., Li, J., Wu, C., Cao, C., Wang, Y., Zheng, J., Secrest, J., Li, Y., Wang, Y., Li, H., Li, N., and Zhang, R.: Particle acidity and sulfate production during severe haze events in China cannot be reliably inferred by assuming a mixture of inorganic salts, Atmos. Chem. Phys., 18, 10123–10132, doi: 10.5194/acp-18-10123-2018, 2018.

Wang, L., Khalizov, A. F., Zheng, J., Xu, W., Ma, Y., Lal, V. and Zhang, R.: Atmospheric nanoparticles formed from heterogeneous reactions of organics, Nat. Geosci., 3(4), 238–242, doi:10.1038/ngeo778, 2010.

Wang, M., Chen, D., Xiao, M., Ye, Q., Stolzenburg, D., Hofbauer, V., Ye, P., Vogel, A. L., Mauldin, R. L., Amorim, A., Baccarini, A., Baumgartner, B., Brilke, S., Dada, L., Dias, A., Duplissy, J., Finkenzeller, H., Garmash, O., He, X.-C., Hoyle, C. R., Kim, C., Kvashnin, A., Lehtipalo, K., Fischer, L., Molteni, U., Petäjä, T., Pospisilova, V., Quéléver, L. L. J., Rissanen, M., Simon, M., Tauber, C., Tomé, A., Wagner, A. C., Weitz, L., Volkamer, R., Winkler, P. M., Kirkby, J., Worsnop, D. R., Kulmala, M., Baltensperger, U., Dommen, J., El-Haddad, I., and Donahue, N. M.: Photo-oxidation of Aromatic Hydrocarbons Produces Low-Volatility Organic Compounds, Environ. Sci. Technol., 54(13), 7911–7921, doi:10.1021/acs.est.0c02100, 2020.

Wang, Y., Khalizov, A., Levy, M., and Zhang, R.: Light absorbing aerosols and their atmospheric impacts, Atmos. Environ., 81, 713-715, doi:10.1016/j.atmosenv.2013.09.034, 2013.

Wang, Y., Lee, K.-H., Lin, Y., Levy, M., and Zhang, R.: Distinct effects of anthropogenic aerosols on tropical cyclones, Nature Clim. Change, 4, 368–373, doi:10.1038/nclimate2144 2014.

Wennberg, P. O., Bates, K. H., Crounse, J. D., Dodson, L. G., McVay, R. C., Mertens, L. A., Nguyen, T. B., Praske, E., Schwantes, R. H., Smarte, M. D., St Clair, J. M., Teng, A. P., Zhang, X., and Seinfeld, J. H.: Gas-Phase Reactions of Isoprene and Its Major Oxidation Products, Chem. Rev., 118, 3337–3390, 2018.

Xue, H., Khalizov, A. F., Wang, L., Zheng, J., and Zhang, R.: Effects of Coating of Dicarboxylic Acids on the Mass−Mobility Relationship of Soot Particles, Environ. Sci. Technol., 43(8), 2787–2792, doi:10.1021/es803287v, 2009.

Yuan, B., Koss, A. R., Warneke, C., Coggon, M., Sekimoto, K. and de Gouw, J. A.: Proton-Transfer-Reaction Mass Spectrometry: Applications in Atmospheric Sciences, Chem. Rev., 117(21), 13187–13229, doi:10.1021/acs.chemrev.7b00325, 2017.

Zhang, D., Lei, W., and Zhang, R.: Mechanism of OH formation from ozonolysis of isoprene: Kinetics and product yields, Chem. Phys. Lett. 358, 171-179, 2002.

Zhang, F., Wang, Y., Peng, J., Chen, L., Sun, Y., Duan, L., Ge, X., Li, Y., Zhao, J., Liu, C., Zhang, X., Zhang, G., Pan, Y., Wang, Y., Zhang, A.L., Ji, Y., Wang, G., Hu, M., Molina, M.J., and Zhang, R.: An unexpected catalyst dominates formation and radiative forcing of regional haze, Proc. Natl. Acad. Sci. USA, 117, 3960-3966, doi/10.1073/pnas.1919343117, 2020.

Zhang, Q., Xu, Y., and Jia, L.: Secondary organic aerosol formation from OH-initiated oxidation of m-xylene: effects of relative humidity on yield and chemical composition, Atmos. Chem. Phys., 19(23), 15007–15021, doi:10.5194/acp-19-15007-2019, 2019.

Zhang, R., Leu, M.T., and Keyser, L.F.: Heterogeneous reactions involving $ClONO_2$, HCl, and HOCl on liquid sulfuric acid surfaces, J. Phys. Chem., 98, 13563-13574, 1994.

Zhang, R., Suh, I., Zhao, J., Zhang, D., Fortner, E. C., Tie, X., Molina, L. T. and Molina, M. J.: Atmospheric New Particle Formation Enhanced by Organic Acids, Science (80-.)., 304(5676), 1487 LP – 1490, doi:10.1126/science.1095139, 2004.

Zhang, R., Wang, L., Khalizov, A. F., Zhao, J., Zheng, J., McGraw, R. L., and Molina, L. T.: Formation of nanoparticles of blue haze enhanced by anthropogenic pollution, Proc. Natl. Acad. Sci. USA, 106, doi:10.1073/pnas.0910125106, 17650-17654, 2009.

Zhang, R., Wang, G., Guo, S., Zamora, M. L., Ying, Q., Lin, Y., Wang, W., Hu, M., and Wang, Y.: Formation of Urban Fine Particulate Matter, Chem. Rev., 115(10), 3803–3855, doi:10.1021/acs.chemrev.5b00067, 2015.

Zhang, R., Johnson, N.M., and Li Y.: Establishing the exposure-outcome relation between airborne particulate matter and children's health, Thorax, 76, doi.org/10.1136/thoraxjnl-2021-217017, 2021.

Zhang, X., Cappa, C. D., Jathar, S. H., McVay, R. C., Ensberg, J. J., Kleeman, M. J., and Seinfeld, J. H.: Influence of Vapor Wall Loss in Laboratory Chambers on Yields of Secondary Organic Aerosol. Proc. Natl. Acad. Sci. U.S.A., 111, 5802−5807, 2014.

734 Zhao, J., and Zhang, R.: Proton transfer reaction rate constants between hydronium ion (H_3O^+) and
735 volatile organic compounds, Atmos. Environ., 38(14), 2177–2185,
736 doi:https://doi.org/10.1016/j.atmosenv.2004.01.019, 2004.

737 Zhao, J., Zhang, R., Fortner, E.C., and North, S.W.: Quantification of hydroxycarbonyls from OH-
738 isoprene reactions, J. Am. Chem. Soc., 126, 2686-2687, 2004.

739 Zhao, J., Zhang, R., Misawa, K., and Shibuya, K.: Experimental product study of the OH-initiated
740 oxidation of m-xylene, J. Photochem. Photobiol. A Chem., 176(1), 199–207,
741 doi:https://doi.org/10.1016/j.jphotochem.2005.07.013, 2005.

742 Zhu, J., Penner, J. E., Lin, G., Zhou, C., Xu, L., and Zhuang, B.: Mechanism of SOA formation
743 determines magnitude of radiative effects, P. Natl. Acad. Sci. USA, 114, 12685–12690,
744 https://doi.org/10.1073/pnas.1712273114, 2017.

745
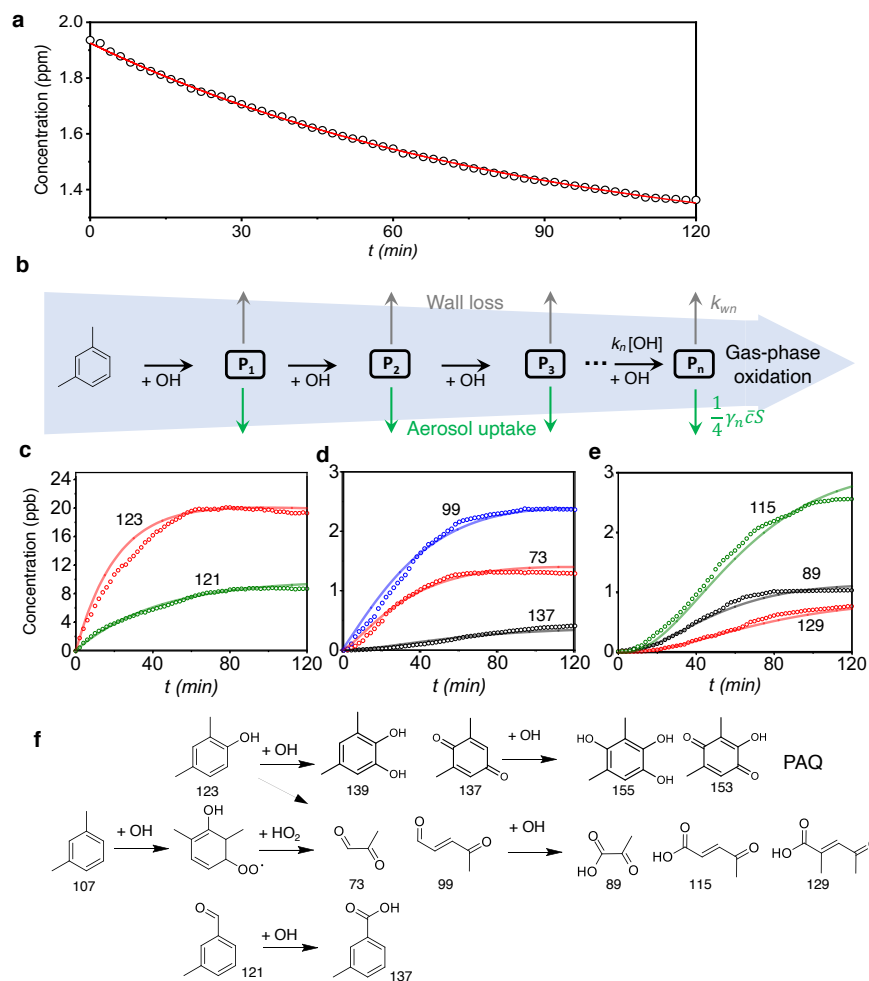
Figure 1. OH-initiated photooxidation of *m*-xylene. (a) Time-dependent concentration of *m*-xylene. The symbols are from the measurements, and the red solid line corresponds to exponential fitting of the *m*-xylene concentration. The initial concentration for *m*-xylene and the estimated steady-state concentration for OH are 1940 ppb and 2.1×10^6 molecules cm^{-3}, respectively, with a bimolecular rate constant of 2.4×10^{-11} cm^3 molecule^{-1} s^{-1}. (b) Schematic representation leading to the multi-generation product, P_n, where n denotes the sequence of OH-initiated oxidation. The black, gray, and green arrows denote the gas-phase oxidation, chamber wall loss, and aerosol uptake, respectively. k_n and kw_n are the rate coefficients for the gas-phase oxidation and wall loss, respectively, γ_n represents the aerosol uptake coefficient, $\bar{c}$ is the thermal velocity, and S is the aerosol surface area. (c-e) Time-dependent gas-phase concentrations of P_1 (c), P_2 (d), and P_3 (e) products. The symbols are from measurements, and the solid curves are simulated according to the tri-exponential kinetics. (f) The gaseous oxidation pathways leading to the detected products. The top row corresponds to the pathways leading to polyhydroxy aromatics/quinones (PAQ). The numbers in (c) to (f) represents the mass to charge ratio (*m/z*). All experiments are carried out for $(NH_4)_2SO_4$ seed particles with 19 ppb NH_3 at 298 K and RH = 70%. Initiation of photooxidation by ultraviolet light occurs at $t = 0$.
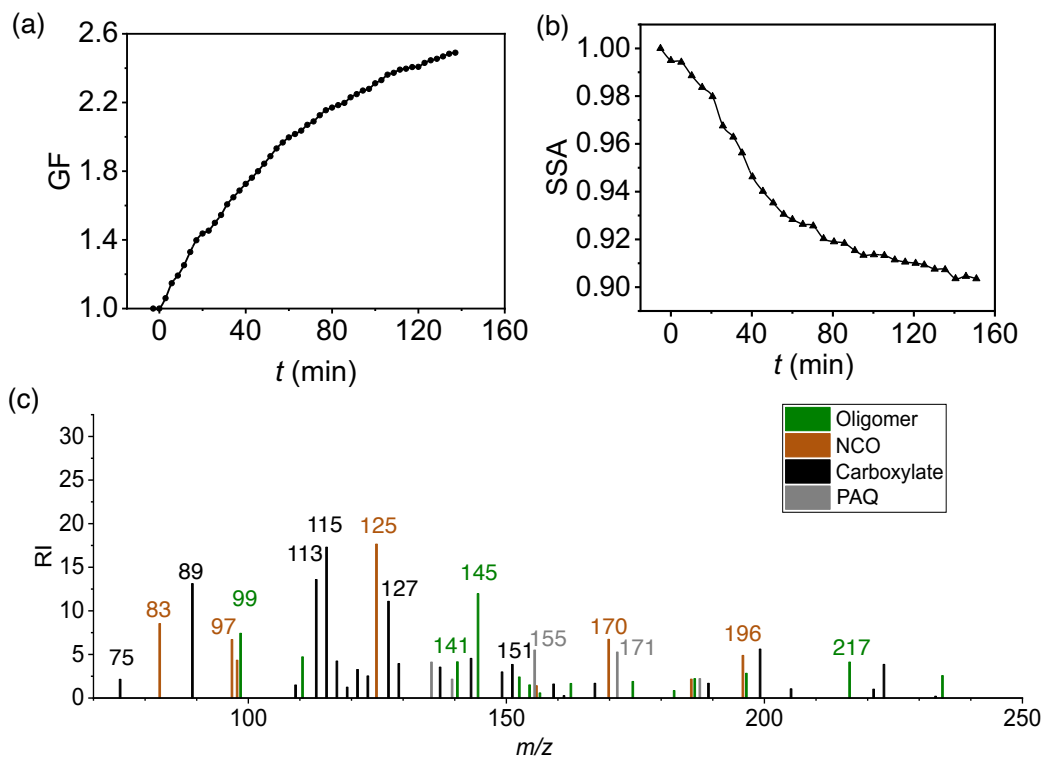
Figure 2. SOA and BrC formation from *m*-xylene photooxidation. Time-dependent growth factor (GF = D_p/D_0, a) and single scattering albedo (SSA, b) of seed particles exposed to *m*-xylene oxidation products. (c) Chemical speciation of aerosol-phase products by TD-ID-CIMS. Initiation of photooxidation by ultraviolet light occurred at *t* = 0. RI denotes the relative intensity for the integrated peak area during thermal desorption. All experiments are carried out for $(NH_4)_2SO_4$ seed particles with 19 ppb NH_3 at 298 K and RH = 70%.
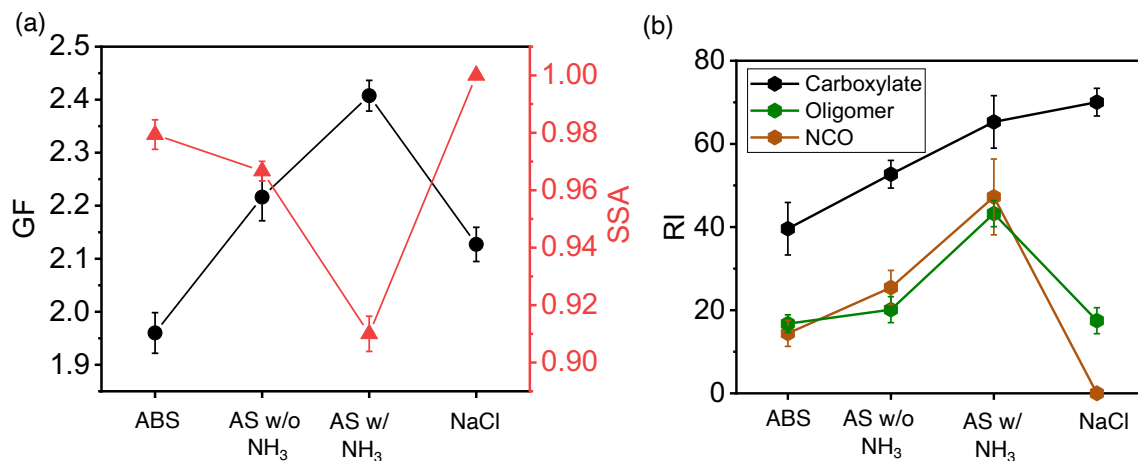
Figure 3. Dependence of SOA/BrC formation on seed particles. (a) GF (black) and SSA (red) at 120 mins of exposure for $(NH_4)_2SO_4$ particles in the presence (AS w/ NH_3) and absence (AS w/o NH_3) of 19 ppb NH_3 and for NH_4HSO_4 (ABS) and NaCl particles in the absence of NH_3. (b) Aerosol-phase relative intensity (RI) for carboxylates (black), oligomers (green), and NCO (brown) on different seed particles. The error bar denotes 1σ of 3 replicated measurements. All particle properties were measured relevant to dry conditions (less than 5% RH) and were dominantly contributed by non-volatile aerosol-phase products.
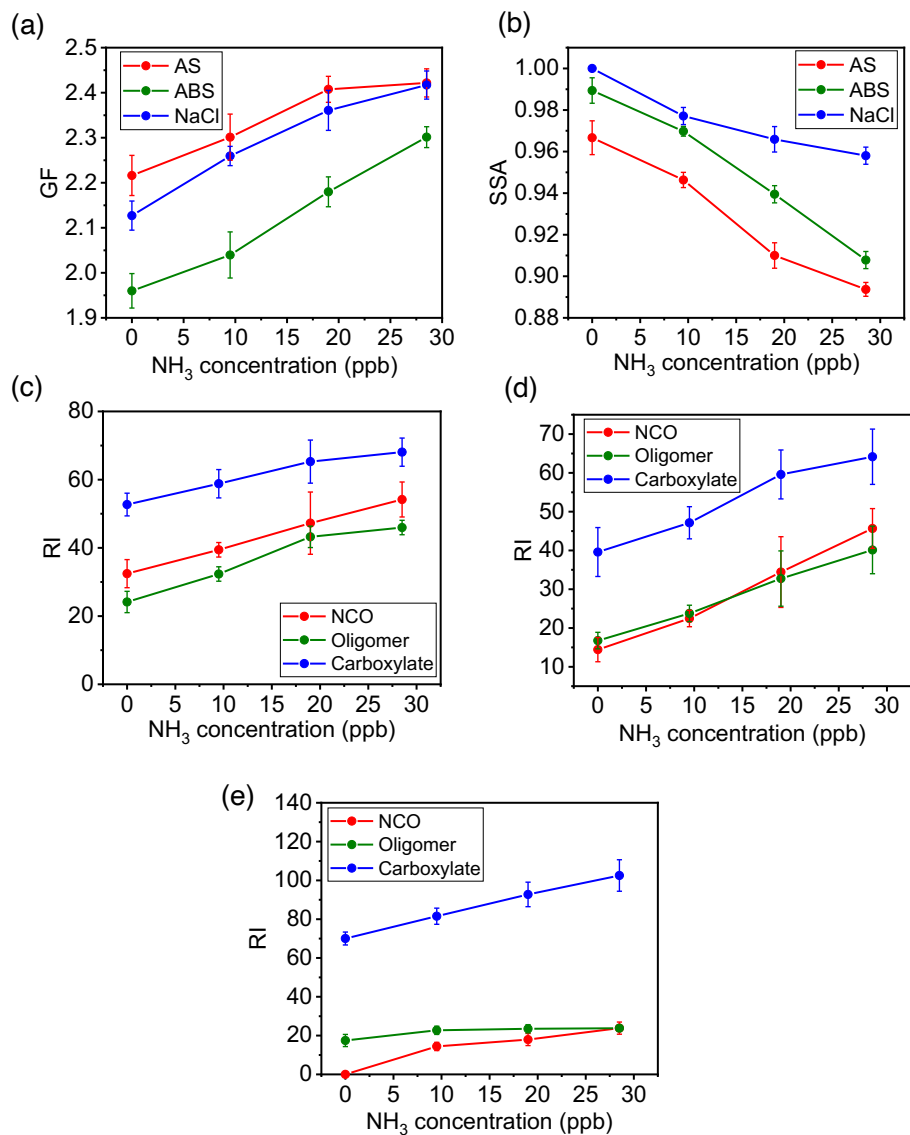
Figure 4. Variation of SOA formation with seed particles and NH_3 concentration. (a,b) growth factor (a) and SSA (b) at t = 120 min with varying NH_3 concentration between 0 and 27 ppb for ammonium sulfate (AS, red), ammonium bisulfate (ABS, green), and sodium chloride (NaCl, blue) seed particles. (c-e) Aerosol-phase mass relative intensity (RI) for NCO (red), oligomers (green), and carboxylates (blue) on AS (c), ABS (d), and NaCl (e) seed particles. The error bar denotes 1σ of 3 replicated measurements.
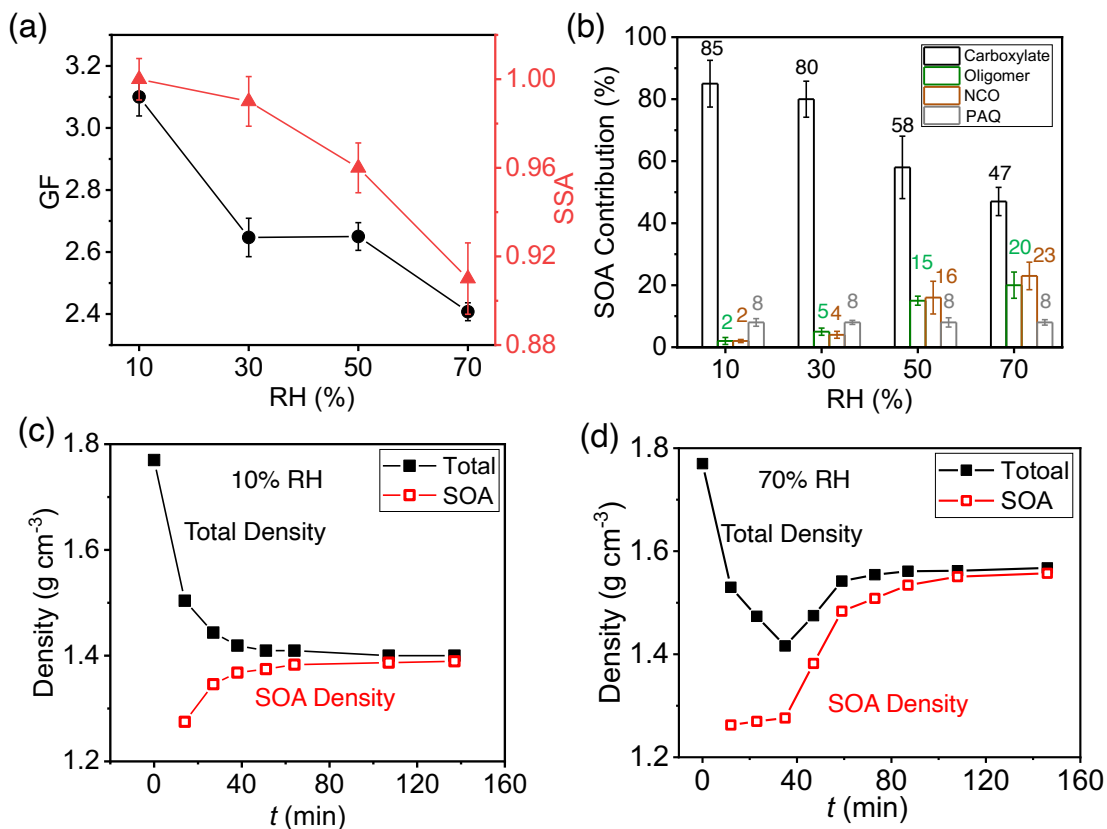
Figure 5. Dependence of SOA/BrC formation on RH. (a) GF (black) and SSA (red) at 120 min with varying RH from 10% to 70%. (b) Contribution of COOs to SOA formation with varying RH from 10% to 70%: carboxylate (black), oligomers (green), NCO (brown), and PAQ (gray) to SOA formation. The number denotes the percentage contribution (%) of each type of aerosol-phase products. (c,d) Time-dependent particle (black) and SOA (red) densities of seed particles exposed to *m*-xylene oxidation products at RH = 10% (c) and 70% (d), respectively. The error bar denotes 1σ of 3 replicated measurements.
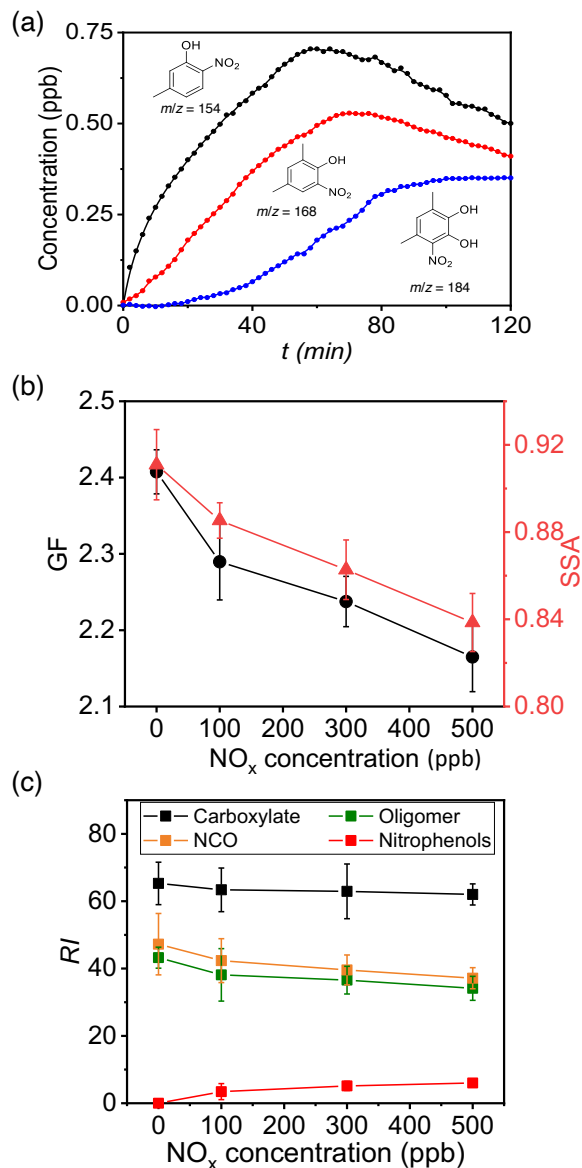
Figure 6. The effects of NO_x. (a) Time-dependent gas-phase concentrations of 5-methyl-2-nitrophenol (black, $m/z = 154$), dimethyl nitrophenol (red, $m/z = 168$), and dihydroxy nitrotoluene (blue, $m/z = 184$). The numbers denote the mass to charge ratio (m/z). Initiation of photooxidation by ultraviolet light occurred at $t = 0$. (b) GF (black) and SSA (red) at 120 min with varying NO_x concentration from 0 to 500 ppb. (h) Dependence of aerosol-phase relative mass intensities (RI) for carboxylates (black), oligomers (green), NCO (brown), and nitrophenols (red) on NO_x concentration for $(NH_4)_2SO_4$ seed particles with 19 ppb NH_3 at RH = 70%. The error bar denotes 1σ of 3 replicated measurements.
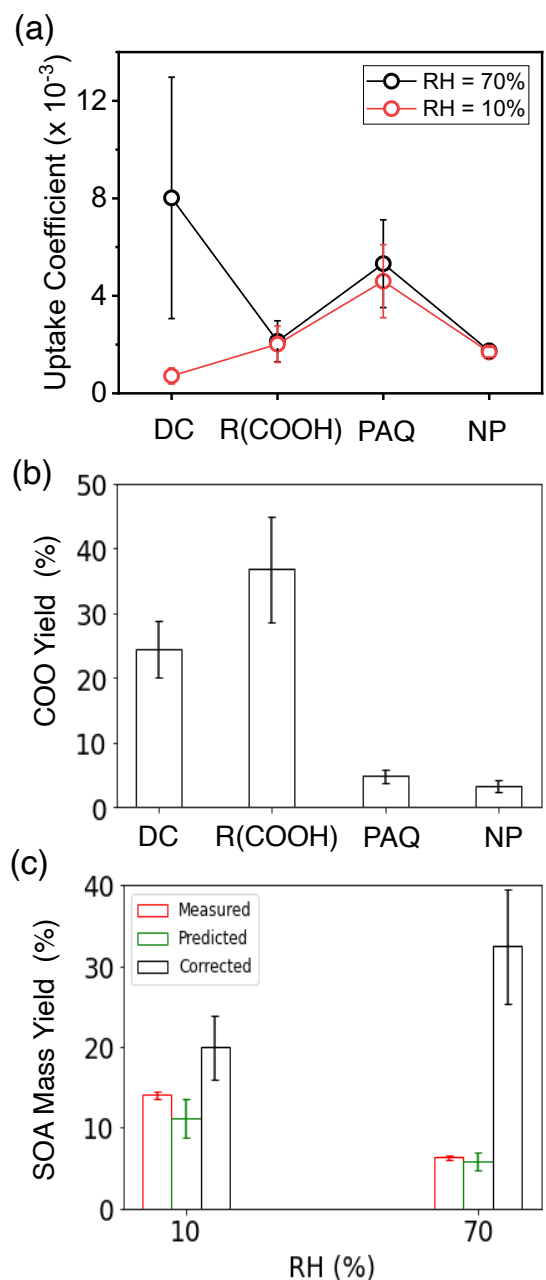
Figure 7. Uptake coefficient, COO yield, and SOA mass yield. (a) Average uptake coefficients (γ) for different types of COOs at 10% (red) and 70% (black) RH for $(NH_4)_2SO_4$ seed particles with 19 ppb NH_3 at 298 K. (b) COO yields: dicarbonyls, organic acids, polyhydroxy aromatics/quinones, and nitrophenols are represented by DC, $R(COOH)_n$, PAQ, and NP, respectively. (c) SOA mass yields at 10% (left columns) and 70% RH (right). The red, green, and black columns represent the measured, predicted, and corrected (for wall loss) SOA mass yields according to eq. 19-22. All experiments are carried out for 14 μg m^{-3} $(NH_4)_2SO_4$ seed particles with 19 ppb NH_3 at 298 K. The error bars denote the 1σ of 3 replicated measurements or by accounting for error propagation of the measured parameters.

819 **Table 1. Summary of experimental conditions.**

Experiment #	Seed particle	NH_3 concentration (ppb)	NO_x concentration (ppb)	RH
Exp. 1	AS	19	0	70%
Exp. 2	AS	0	0	70%
Exp. 3	ABS	0	0	70%
Exp. 4	NaCl	0	0	70%
Exp. 5	AS	9.5	0	70%
Exp. 6	AS	28.5	0	70%
Exp. 7	ABS	9.5	0	70%
Exp. 8	ABS	19	0	70%
Exp. 9	ABS	28.5	0	70%
Exp. 10	NaCl	9.5	0	70%
Exp. 11	NaCl	19	0	70%
Exp. 12	NaCl	28.5	0	70%
Exp. 13	AS	19	0	10%
Exp. 14	AS	19	0	30%
Exp. 15	AS	19	0	50%
Exp. 16	AS	19	100	70%
Exp. 17	AS	19	300	70%
Exp. 18	AS	19	500	70%

820

821